Front. Mech. Eng. 2023, 18(3): 35
https://doi.org/10.1007/s11465-023-0751-5

RESEARCH ARTICLE

Sub-nanometer finishing of polycrystalline tin by inductively coupled plasma-assisted cutting

Peng LYU[a], Min LAI (✉)[a], Yifei SONG[a], Zhifu XUE[a], Fengzhou FANG (✉)[a,b]

[a] *State Key Laboratory of Precision Measuring Technology & Instruments, Laboratory of MicroNano Manufacturing Technology—MNMT, Tianjin University, Tianjin 300072, China*
[b] *Centre of MicroNano Manufacturing Technology—MNMT-Dublin, School of Mechanical & Materials Engineering, University College Dublin, Dublin 4, Ireland*

✉ *Corresponding authors. E-mails: laimin@tju.edu.cn (Min LAI); fzfang@tju.edu.cn (Fengzhou FANG)*

ABSTRACT Polycrystalline tin is an ideal excitation material for extreme ultraviolet light sources. However, the existence of grain boundary (GB) limits the surface roughness of polycrystalline tin after single-point diamond turning (SPDT). In this work, a novel method termed inductively coupled plasma (ICP)-assisted cutting was developed for the sub-nanometer finishing of polycrystalline tin. The relationship between ICP power, processing time, and modification depth was established by thermodynamic simulation, and the fitted heat transfer coefficient of polycrystalline tin was 540 W/(m^2·K). The effects of large-thermal-gradient ICP treatment on the microstructure of polycrystalline tin were studied. After 0.9 kW ICP processing for 3.0 s, corresponding to the temperature gradient of 0.30 K/μm, the grain size of polycrystalline tin was expanded from a size of approximately 20–80 μm to a millimeter scale. The Taguchi method was used to investigate the effects of rotational speed, depth of cut, and feed rate on SPDT. Experiments conducted based on the ICP system indicated that the plasma-assisted cutting method promoted the reduction of the influence of GB steps on the finishing of polycrystalline tin, thereby achieving a surface finish from 8.53 to 0.80 nm in *Sa*. The results of residual stress release demonstrated that the residual stress of plasma-assisted turning processing after 504 h stress release was 10.7 MPa, while that of the turning process without the ICP treatment was 41.6 MPa.

KEYWORDS plasma-assisted cutting, polycrystalline tin, single-point diamond turning, surface roughness

1 Introduction

Soft and low-melting-point metal polycrystalline tin has a wide application prospect in various fields, such as scientific instruments and physical experiments. In float polishing of sapphire, the polishing disc made of tin can be used to achieve the sapphire surface roughness of 0.08 nm in root mean square [1]. In the research of soft X-ray light sources, metallic tin is used as the target of an extreme ultraviolet light source, and its sharp emission peak at 13.5 nm makes it an attractive laser plasma light source [2,3]. The research on the impact compression of tin micromaterial injection enables the characterization of the diagnosis of material dynamic characteristics and inhibition sources in applications, such as inertial confinement fusion [4,5]. The tin surface with low roughness and residual stress strongly influences the float polishing accuracy, laser plasma light source stability, and Rayleigh–Taylor instability [6].

Single-point diamond turning (SPDT) is a promising technology for the high surface quality machining of various materials, which has a potential to achieve a surface finish down to atomic and close-to-atomic scale (ACS) [7,8]. However, the ultraprecision turning process for polycrystalline tin, which has a melting point of 505 K [9] and Mohs hardness of 1.5 [10], has not been reported by far. The strong plasticity of soft metal tin induces plastic deformation easily in the micro- and nanoscale machining process, resulting in a stick-slip phenomenon with friction between the tool interface and soft metal materials [11]. In addition, the grain boundaries (GBs) and orientations of polycrystalline metals affect the machined surface quality significantly. Previous research on SPDT of soft metals, such as Al and Cu, presented the achieved surface finish at ACS. When high-speed diamond cutting was used to process

Received November 23, 2022; accepted March 5, 2023

polycrystalline oxygen-free Cu and lead brass ($CuZn_{39}Pb_3$), the surface roughness after cutting was limited by the grain structure of metal materials. Given that different grains have various crystal orientations, the elastic-plastic recovery of each grain after cutting varied. The resulting GB steps deteriorated the surface quality, and the optimal step height was 8 nm [12,13]. By regulating the ultraprecision cutting parameters of polycrystalline Cu, Wang et al. [14] found that the influence of polycrystalline Cu GB on the surface quality cannot be completely eliminated, and a surface roughness in *Ra* less than 1 nm was attained locally. The negative effects of GBs on the machined surface roughness of tin, as a typical soft and polycrystalline metal, during SPDT are predictable. Regulating the grain size of polycrystalline tin is a potential method to lessen the GB effect on SPDT-machined surfaces.

Grain growth would occur at a high temperature in polycrystalline materials. The GB of polycrystals is in a high-energy state, and the temperature gradient could cause an energy imbalance between the grains, which is the driving force for GB migration [15,16]. Small grains would merge into large grains at high temperature gradient to reduce the total area of high-energy GBs [17]. Xu et al. [18] reported the growth of meter-scale two-dimensional single-crystal Cu (111) by slowly passing the industrial polycrystalline Cu through a hot zone (1303 K). In selective laser melting, a directional heat flow gradient is formed in the laser molten pool, which makes the liquid alloy in the molten pool prone to directional solidification and formation of epitaxially grown coarse columnar crystals, such as titanium alloy β-columnar crystals [19], nickel-based alloy columnar crystals [20], and iron-based alloy columnar crystals [21]. These epitaxial columnar crystals can reach the centimeter level. Li et al. [22] used electron beam selective melting (EBSM) to produce nickel-based superalloy single crystals. Helmer et al. [23] proposed that the large single crystals in EBSM may be controllable by a suitable temperature gradient [24]. These studies showed that small grains could be recrystallized into larger grains by employing high temperature gradient, and the selection of appropriate temperature gradient is the key to realizing grain amplification. However, the devices used in the above process are complex and expensive for a quick large-area high-thermal-gradient treatment of polycrystalline tin surface in the atmosphere. Compared with the above process, inductively coupled plasma (ICP) has a simple structure, low environmental requirements, and stable large-area treatment, making it an ideal large-thermal-gradient source [25]. Moreover, compared with the carbon dioxide laser and oxyhydrogen flame heating methods widely used at present, ICP require neither surface pretreatment to increase laser absorption nor combustible gas combustion. Argon (Ar) for excitation is cheap and safe [26,27]. Therefore, ICP is expected to serve as an effective medium for increasing the grain size of polycrystalline tin.

In this study, an induction discharge plasma-assisted cutting (PaC) method was proposed to reduce the influence of GB steps on the surface roughness of polycrystalline tin during SPDT. Through the large thermal gradient of ICP, the polycrystalline tin grains in the area were expanded, which decreased the number of GBs on the surface of polycrystalline tin. Then, the influence of GB steps on the surface quality during SPDT was eliminated. Finally, a polycrystalline tin surface that was ultrasmooth and had minimal residual stress and surface roughness in *Sa* less than 1 nm was generated.

2 Principle and methods

2.1 Principle of PaC

The proposed PaC is depicted schematically in Fig. 1. Atmospheric pressure ICP is a dense ionized plasma source with high free radical density and gas temperature [28]. First, the polycrystalline tin sample was subjected to a large-thermal-gradient heat treatment through high-power ICP to form the grain fusion layer. Then, the grain fusion layer was fixed through the cooling of compressed air to reduce the influence of GB on the surface roughness. Chemically stable gas Ar was used as the plasma ignition gas [29,30]. Thus, surface oxidation and other chemical reactions did not occur during the large-thermal-gradient heat ICP treatment process. Afterward, the grain amplification layer obtained by SPDT or other cutting methods was processed to obtain the ideal surface quality, which reduced the influence of GB on the quality of the machined surface effectively.

2.2 Simulation methods

To obtain the temperature distribution of the ICP jet, we used the methods of coupling magnetic field, fluid heat transfer, and laminar flow for numerical simulation [31,32]. The model was simplified properly, and the main governing equations are listed as follows.

Maxwell's equations were used to describe the effect of the magnetic field and heat transfer equation of fluids:

$$\rho C_{\mathrm{p}} \frac{\partial T}{\partial t} + \rho C_{\mathrm{p}} \boldsymbol{u} \cdot \nabla T + \nabla \cdot \boldsymbol{q} = Q + Q_{\mathrm{p}} + Q_{\mathrm{vd}}, \tag{1}$$

$$\boldsymbol{q} = -k \nabla T, \tag{2}$$

where ρ is the plasma's fluid density, C_{p} is the plasma's specific heat capacity, T is the plasma temperature, $\boldsymbol{u}$ is the plasma's velocity vector, $\boldsymbol{q}$ is the plasma's heat flux conductivity vector, Q is the source of heat, Q_{p} is the work of pressure, Q_{vd} is the work of viscous dissipation, and k is a measure of thermal conductivity.

The laminar flow formula is as follows:

$$\rho(\boldsymbol{u}\cdot\nabla)\boldsymbol{u}=\nabla\cdot\left[-p\boldsymbol{I}+\mu\left(\nabla\boldsymbol{u}+(\nabla\boldsymbol{u})^{\mathrm{T}}\right)-\frac{2}{3}\mu(\nabla\cdot\boldsymbol{u})\boldsymbol{I}\right]+\boldsymbol{F}, \tag{3}$$

$$\nabla\cdot(\rho\boldsymbol{u})=0, \tag{4}$$

where p is a measure of pressure, $\boldsymbol{I}$ is the matrix of identity, μ indicates the dynamic viscosity, and $\boldsymbol{F}$ indicates the Lorentz force.

Figure 2(a) shows the two-dimensional axisymmetric simplified model of the ICP quartz tube. The size of the ICP torch was the same as that used in actual processing, and the model's initial temperature was 300 K. Through Eqs. (1)–(4), the temperature distribution of the plasma in the ICP quartz tube under different power excitations can be simulated, and the temperature distribution at the location where the sample was placed can further be obtained. As the heat source of the ICP torch heating polycrystalline tin sample, section temperature distribution was input into the tin thermodynamic transfer model. Table 1 summarizes the ICP simulation parameters.

When the polycrystalline tin sample was heated under the large temperature gradient of the ICP device, the surface layer was gradually heated up and melted. The depth of the melting layer can be predicted accurately by controlling the processing power and time. A simplified heat transfer model of polycrystalline tin was established, and its governing equations were derived as follows.

When the heat source acted on the tin surface, the heat was transferred to the interior of the sample. Assuming that all domains were isotropic continuous media, the

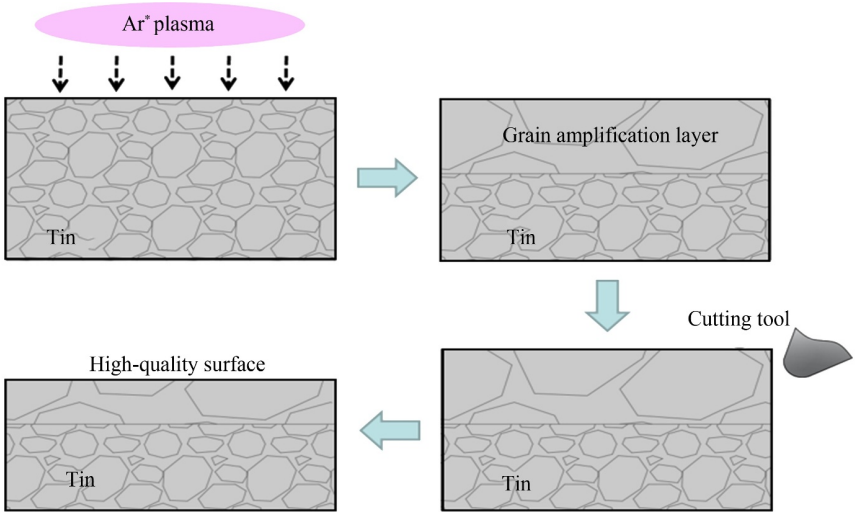

Fig. 1 Principle of plasma-assisted cutting treatment for polycrystalline tin. Ar: argon.

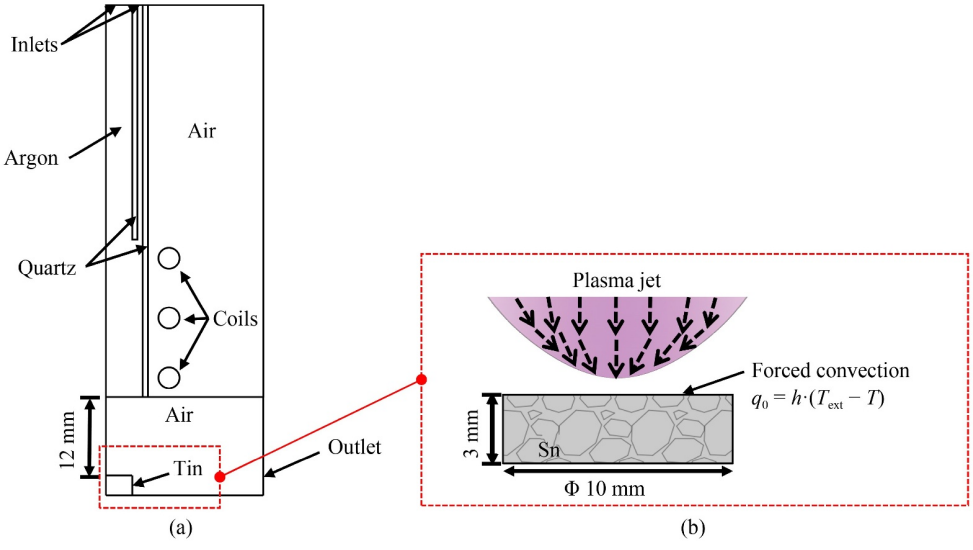

Fig. 2 Schematic of the simulation: (a) atmospheric inductively coupled plasma torch geometry model and (b) heat transfer from inductively coupled plasma to tin.

Table 1 ICP simulation parameters

Parameters	Value
Frequency	27.12 MHz
Power	0.4, 0.6, 0.7, 0.8, 0.9, and 1.0 kW
Excitation gas and flow	Ar, 2 L/min
Cooling gas and flow	Ar, 15 L/min
Initial temperature	300 K

heat transfer equation is as follows:

$$\rho_1 C_{p_1} \frac{\partial T_1}{\partial t} + \rho_1 C_{p_1} \boldsymbol{u}_1 \cdot \nabla T_1 + \nabla \cdot \boldsymbol{q}_1 = Q_1 + Q_{ted}, \quad (5)$$

$$\boldsymbol{q}_1 = -k_1 \nabla T_1, \quad (6)$$

where ρ_1 is the density of tin, C_{p_1} is tin's specific thermal capacity, T_1 is the tin temperature, $\boldsymbol{u}_1$ is tin's velocity vector, $\boldsymbol{q}_1$ is the vector of heat flux conductivity, Q_1 is the heat source of tin, Q_{ted} is the thermoelastic damping, and k_1 is the thermal conductivity of tin.

The heat flux transferred to tin was computed as follows:

$$-\boldsymbol{n} \cdot \boldsymbol{q}_1 = q_0, \quad (7)$$

$$q_0 = h \cdot (T_{ext} - T_1), \quad (8)$$

where $\boldsymbol{n}$ is the normal vector, q_0 means internal heat flow, h is the coefficient of heat transfer, and T_{ext} is the ICP action section temperature.

Figure 2(b) displays the heat transfer model. The basic size of polycrystalline tin was the same as that of the actual processing sample. The cross-section temperature T_{ext} distribution was obtained by function fitting through the least square method. The melting process of polycrystalline tin is very complex, and no standard data are available for the heat transfer coefficient of polycrystalline tin. To simplify the heat transfer model, we determined the maximum temperature of the tin surface after processing by using an infrared thermal camera (Guide Infrared ThermoPro 8s). The fitting heat transfer coefficient h of polycrystalline tin was calculated by the maximum temperature. The melting region was identified as the region where the temperature exceeded the melting point in the model. Finally, the processed polycrystalline tin cross-section samples were prepared to verify the accuracy of the fitting heat transfer coefficient.

2.3 Experimental approach

Figure 3 shows the ICP thermal treatment device used on the equipment. The inner diameter of the outermost quartz tube of the plasma torch was 14 mm, and Ar was supplied to the quartz tube through the gas path of two channels. The second layer of quartz tube supplied 2 L/min Ar to excite the induced plasma discharge. Ar was introduced into the outermost quartz tube to cool the quartz tube. The amount of gas introduced during plasma excitation was 15 L/min. The quartz tube was placed at the center of the induction coil, which was installed on the matcher. During the machining process, the whole device was powered by a radio frequency (RF) power supply (27.12 MHz, 2000 W). Stable Ar plasma was generated under the excitation of an electric spark ignition device, and the tin sample was moved to the machining area through an electric displacement table and cooled in situ after machining. The polycrystalline tin sample used in the experiment had 10 mm diameter and 3 mm thickness.

The PaC treatment for polycrystalline tin can be divided into two steps, namely, plasma thermal treatment and ultraprecision SPDT, which are optimized separately. The magnitude of the thermal gradient was the key parameter

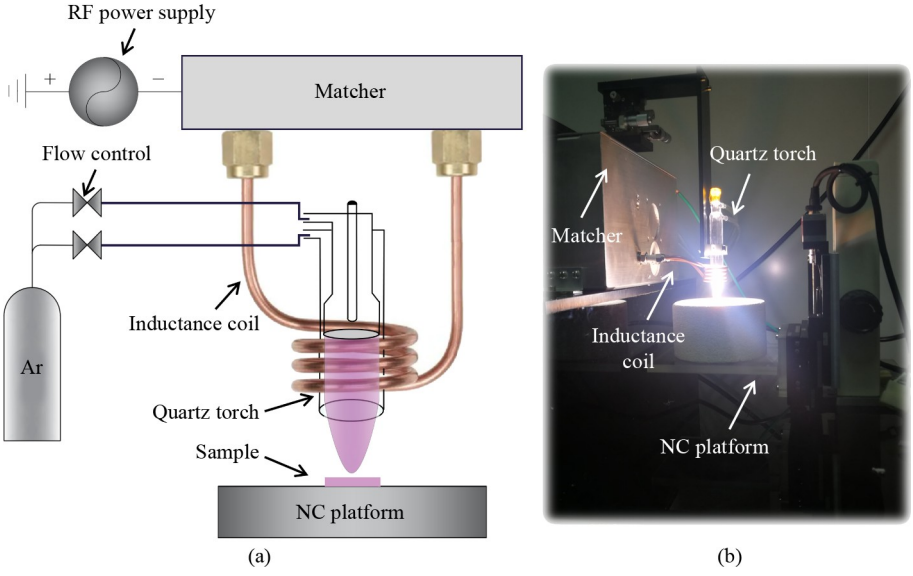

Fig. 3 (a) Schematic and (b) photograph of the inductively coupled plasma setup. Ar: argon, RF: radio frequency.

that modified the solidification microstructures. Different temperature gradients were obtained by changing the plasma power, and the feasibility of PaC was verified by SPDT experiments with the same optimized parameters. The tool nose radius was 500 μm. The cut depth was set to 2 μm, the rotational speed was 1000 r/min, and the feed rate was 2 μm/r. Through the comparison of surface roughness in *Sa*, the appropriate plasma thermal treatment power was selected.

In this work, the Taguchi method was used to investigate the SPDT optimal parameters of polycrystalline tin, which offered an effective systematic approach to optimize designs in terms of quality, performance, and cost [33]. The orthogonal array was used to design the experimental settings. The optimal machining parameters were obtained through three factors with three levels of rotational speed, cut depth, and feed rate, as shown in Table 2.

Table 2 Orthogonal parameters and corresponding values

Level	Rotational speed/(r·min^{-1})	Feed rate/(μm·r^{-1})	Cut depth/μm	Blank group
Level 1	1000	0.9	0.6	1
Level 2	2000	1.8	1.0	2
Level 3	3000	2.7	2.0	3

The blank group was created for analysis of variance (ANOVA) and inadvertent error separation. The early trials determined the level values of the factors. The L_9 (3^4) standard orthogonal array was chosen and used in the tests. The surface roughness of the samples was measured using a white light (WL) interferometer (Veeco, NT9300) with a 20× objective lens and a 1× eyepiece. The measurement area was set to 315 μm × 236 μm. To reduce the influence of inadvertent mistakes, the surfaces were measured 5 times in each group. The surface roughness in *Sa* of the samples was utilized to examine the influence of orthogonal experiment factors on the surface quality of polycrystalline tin.

3 Results and discussion

3.1 Optimization of ICP parameters

The temperature after ICP excitation was directly related to the excitation RF power. Six groups with RF powers of 0.4, 0.6, 0.7, 0.8, 0.9, and 1.0 kW were set to explore the heat source distribution of different powers on the surface of polycrystalline tin. Figure 4 depicts the simulation result. The plasma temperature increased with the increase in power, and the maximum temperature could reach 1500 K at 1 kW power.

The section temperature 0.1 mm above the sample surface was cut at the bottom of the model to obtain the input heat source of the heat transfer model, and the Gaussian function was used to fit the section temperature [34]. Fitting was calculated using the least square method,

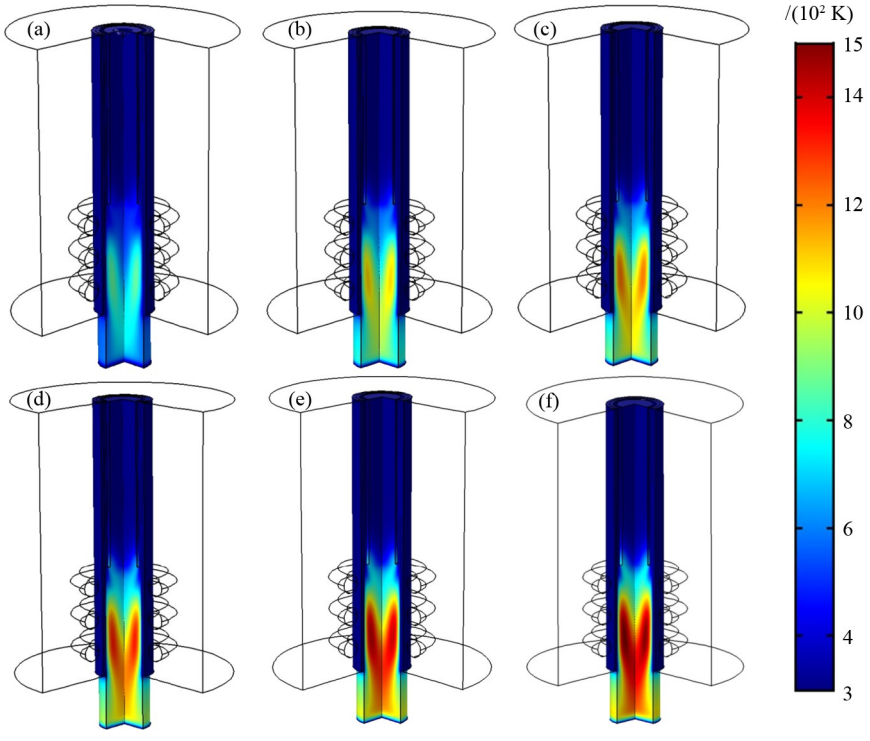

Fig. 4 Temperature simulation of the inductively coupled plasma torch: (a) 0.4 kW, (b) 0.6 kW, (c) 0.7 kW, (d) 0.8 kW, (e) 0.9 kW, and (f) 1.0 kW.

and the function expression is as follows:

$$T_{\text{ext}} = A \cdot \exp\left(-\frac{x^2+y^2}{2\sigma^2}\right) + B, \tag{9}$$

where A is the height of Gaussian function, B is the offset of the Gaussian function along the y-axis, σ is the standard deviation of the Gaussian function, x is the horizontal coordinate, y is the vertical coordinate, and the origin is at the center of the section. If the initial difference between the central maximum temperature in the heat transfer model and the sample bottom temperature was selected, then the initial thermal gradient of each group can be calculated. The formula is as follows:

$$GranT = \frac{T_{\text{ext0}} - T_{\text{bottom}}}{d}, \tag{10}$$

where $GranT$ is the initial temperature gradient in K/μm, T_{ext0} is the central temperature of the heat source, and T_{bottom} is the bottom temperature of polycrystalline tin (300 K).

Table 3 shows the coefficients and thermal gradient results after fitting the six groups of heat sources. With the use of 900 W power to verify the accuracy of Gaussian fitting, the section temperature and error distributions after Gaussian fitting were obtained (Fig. 5). The interpolation between the function expression obtained by Gaussian fitting and the simulation results was within 10 K, which was mainly concentrated on the edge of the section, and the other position errors were within 3 K. This deviation was acceptable compared with the results of the section temperature at 1 kK, in which the fitting errors of other groups were also within 10 K, proving the fitting accuracy.

Table 3 Fitted coefficients and thermal gradient in each group

Power/kW	A	B	σ	$GranT$/(K·μm^{-1})
0.4	751.037	−68.889	12.432	0.12
0.6	262.726	660.779	5.411	0.21
0.7	250.095	770.328	4.968	0.24
0.8	243.535	860.880	4.671	0.27
0.9	246.601	937.824	4.472	0.30
1.0	256.610	1004.079	4.350	0.32

The heat transfer simulation process needed not only a heat source equation but also the acquisition of the heat transfer coefficient (h) of polycrystalline tin. To simplify the simulation modeling, we assumed the heating transfer process as homogeneous and ignored the phase transformation in the melting process. The heat transfer coefficient h was fitted by observing the maximum surface temperature after the treatment time at specific power (0.9 kW for 3.0 s). Figure 6(a) demonstrates that the tin's central temperature was 511.9 K. When the above conditions were introduced into the thermodynamic model, the fitted heat transfer coefficient h was 540 W/(m^2·K). Figure 6(b) shows the temperature distribution simulation of the polycrystalline tin section after heating at 0.9 kW for 3.0 s. The central depth at which the melting point of tin was surpassed was 1.3 mm.

The cross sections of the modified polycrystalline tin sample at 0.9 kW for 3.0 s and the unmodified sample were polished to observe the thickness of the modified layer. The characterization of the polycrystalline tin cross section is shown in Fig. 7. Figures 7(a) and 7(e) display the laser confocal microscope observation images (Olympus, OLS 4000). Figures 7(b), 7(f), and 7(i) show the images obtained by scanning electron microscopy (SEM, Zeiss GeminiSEM 500). Figures 7(c), 7(g), and 7(j) present the electron backscatter diffraction (EBSD) images, and Figs. 7(d), 7(h), and 7(k) present the GB images.

Figure 7(a) shows that the unmodified polycrystalline tin presented many large GBs with a size of

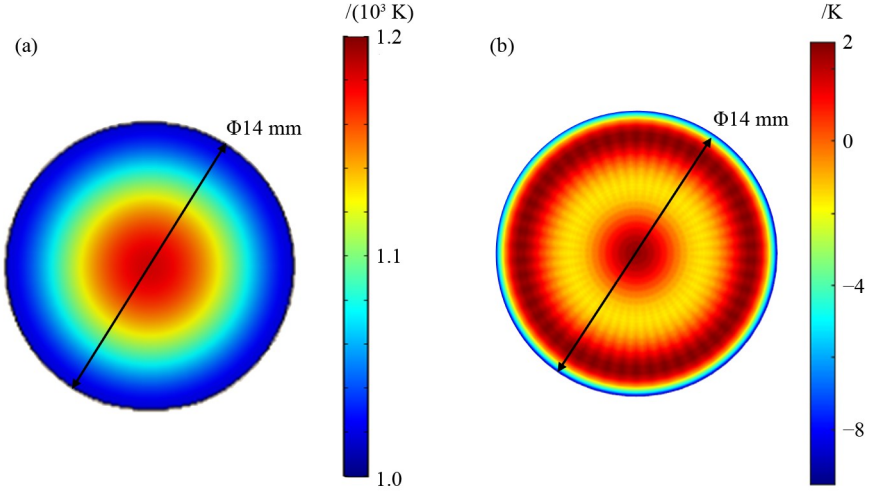

Fig. 5 (a) Section temperature distribution at 900 W and (b) error distribution after Gaussian fitting.

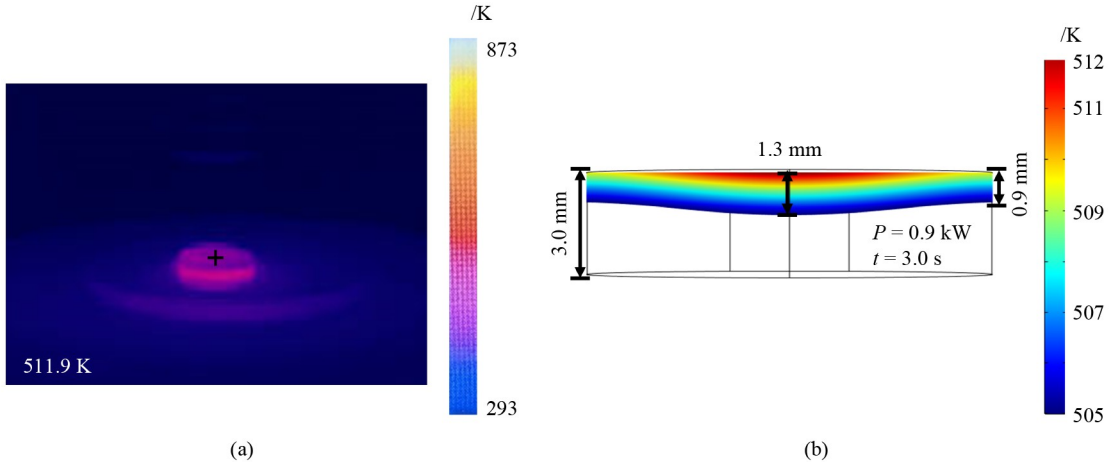

Fig. 6 (a) Infrared thermal image of polycrystalline tin after inductively coupled plasma treatment at 0.9 kW for 3.0 s and (b) section of polycrystalline tin in the heat transfer simulation at 0.9 kW for 3.0 s.

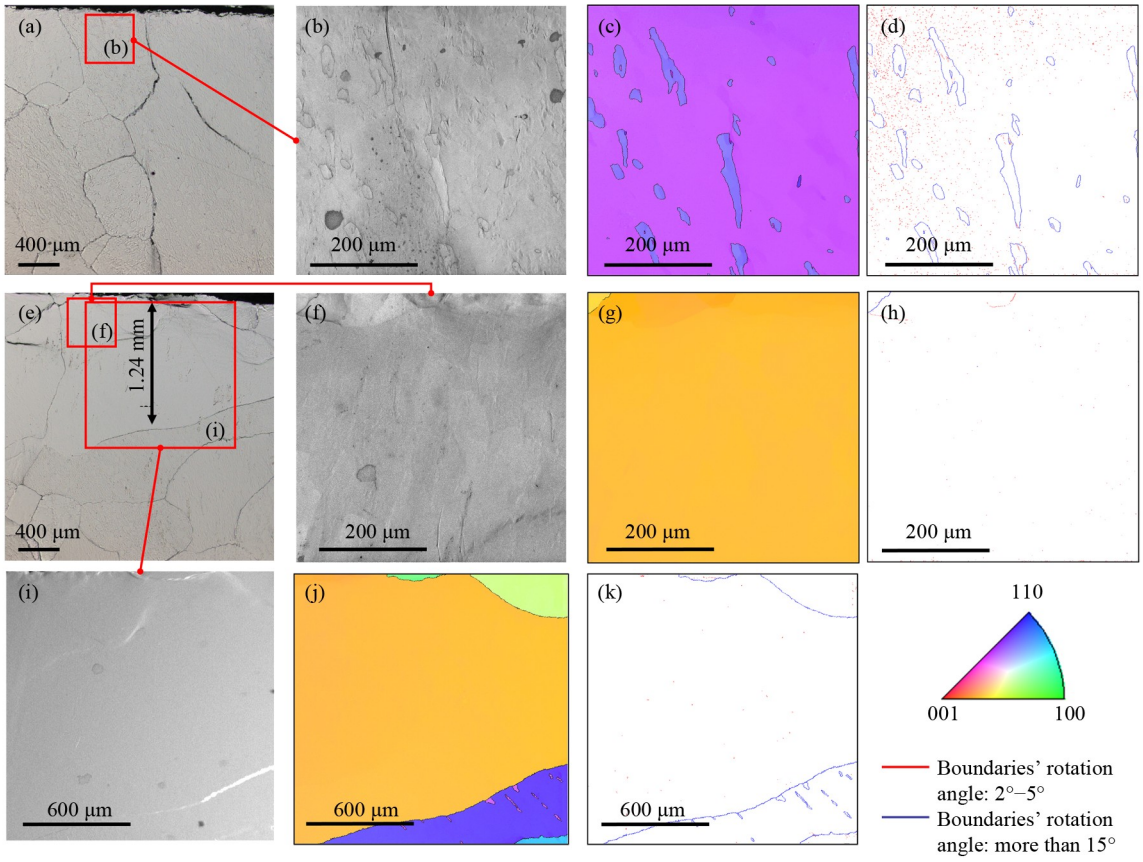

Fig. 7 Characterization of polycrystalline tin cross section: (a) laser confocal microscope image of the unmodified sample, (b) scanning electron microscopy (SEM) image of the 500 μm × 500 μm area in (a), (c) electron backscatter diffraction (EBSD) inverse pole figure map of the same surface in (b), (d) EBSD grain boundary map of the same surface in (b), (e) laser confocal microscope image of the modified sample, (f) SEM image of the 500 μm × 500 μm area in (e), (g) EBSD inverse pole figure of the same surface in (f), (h) EBSD grain boundary map of the same surface in (f), (i) SEM image of the 1500 μm × 1500 μm area in (e); (j) EBSD inverse pole figure of the same surface in (i), and (k) EBSD grain boundary map of the same surface in (i).

approximately 1 mm. Meanwhile, Figs. 7(b) and 7(c) show a large number of small GBs with a size from 20 to 80 μm, and the boundary rotation angle between the small and large grains was greater than 15°, which might be caused by the random orientation distribution in the main growth directions during the preparation of polycrystalline tin [35,36]. Figure 7(d) indicates misorientations with boundary rotation angles of 2°–5° inside large grains.

These GBs and misorientations aggravated the surface roughness of polycrystalline tin during SPDT.

The large GB close to the sample surface was further expanded and could reach about 2 mm in the transverse direction in Fig. 7(e). The modified depth at the center was 1.24 mm, and the internal small GB disappeared completely. The polycrystalline tin may be similar to polycrystalline Cu in terms of the numerous preferential nucleation center directions in the grains, and the orientation deviation inside the large particles was eliminated during the large-thermal-gradient processing [37,38]. However, given the lack of single nucleation center guidance, obtaining a complete single crystal phase was difficult. Thus, the size of large grains could be further increased instead of forming a single crystal phase [20]. The modified depth in Fig. 7(e) at the same position (the center vertical line position of the sample) was close to the simulation melting area depth of 1.3 mm in Fig. 6, which proved that the thermodynamic simulation model could guide the correspondence between the depth of the modified layer and processing time. However, given the randomness of large-grain distribution, the actual processing results were not centrosymmetric, which was different from the prediction uniform model. As displayed in Fig. 7(e), the depths of the modified layer on the left and right sides were different, and such findings may be closely related to the complex process of GB fusion and the initial state of grains. Similarly, a 500 μm × 500 μm area close to the modified tin surface was selected for SEM and EBSD characterization. Figures 7(f) and 7(g) present a single crystalline structure without the GBs of small grains in Figs. 7(b) and 7(c). The misorientations were also effectively removed, as shown in Fig. 7(h).

Figures 7(i), 7(j), and 7(k) show the characterization results at 1500 μm × 1500 μm. The boundary between the modified and unmodified layers presented an irregular shape, and the modified region exhibited a good uniformity, as shown in Figs. 7(i) and 7(j). Different crystal phases only appeared at the interface of large GBs, indicating that plasma modification can effectively remove the small GBs and realize the fusion of large GBs to a certain extent to reduce the effect of GBs on polycrystalline tin surface.

The fitted heat transfer coefficient of 540 W/(m^2·K) was applied to the remaining five groups of plasma treatment power in Table 3, and the fitting modification depth of the central area was approximately 1.3 mm. Figure 8 shows the processing time and simulation results required for each power. With the increase in power, the time required for plasma modification was shortened. Moreover, given that the input heat source was Gaussian distribution, the greatest thickness variation was found between the edge and the middle in Fig. 8(a) for a longer treatment time, and it gradually decreased with the increase in power (Figs. 8(a)–8(e)).

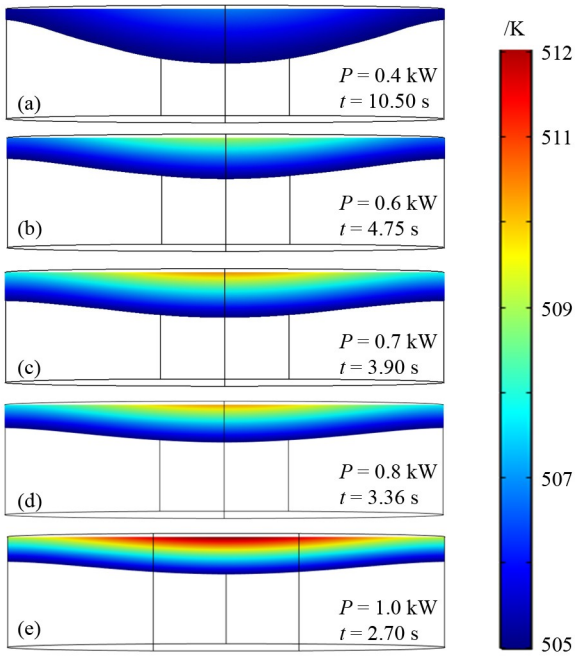

Fig. 8 Section of polycrystalline tin in the heat transfer simulation at different powers. (a) P = 0.4 kW, t = 10.50 s; (b) P = 0.6 kW, t = 4.75 s; (c) P = 0.7 kW, t = 3.90 s; (d) P = 0.8 kW, t = 3.36 s; (e) P = 1.0 kW, t = 2.70 s.

SPDT experiments were carried out on the six groups of samples modified with different powers. Figure 9 depicts the roughness values in *Sa* on the tin surface. The surface roughness of polycrystalline tin without ICP modification was 10.94 nm in *Sa*, and the best was 9.25 nm. A large number of grain fluctuations can be observed on the surface, corresponding to the characterization results in Figs. 7(c) and 7(d). The RF power of ICP modification can be divided into three levels by the surface roughness results. After 0.4 kW ICP modification, the surface quality was improved to a certain extent, the surface roughness in *Sa* was 6.89 nm, and *GranT* was 0.12 K/μm. As for the values of 0.6, 0.7, and 0.8 kW, a slight difference was observed in the machining quality after SPDT, the surface roughness in *Sa* was 5 nm, and the *GranT* range of these three groups of power was 0.21–0.27 K/μm. Lastly, the surface quality of polycrystalline tin modified by 0.9 and 1.0 kW was significantly improved, and the surface roughness values in *Sa* were 2.43 and 2.49 nm, respectively. The optimal measurement point surface roughness in *Sa* was 1.61 nm, the influence of surface GB disappeared, and evident cutting patterns could be observed. The *GranT* of these groups was 0.30 and 0.32 K/μm, respectively.

A laser confocal microscope was used to observe the samples from four groups (0, 0.4, 0.7, and 0.9 kW) in Fig. 9 to explore the connection between *GranT*, grain size, and surface roughness, as shown in Fig. 10. The observed grain size of polycrystalline tin was significantly different. With the increase in temperature

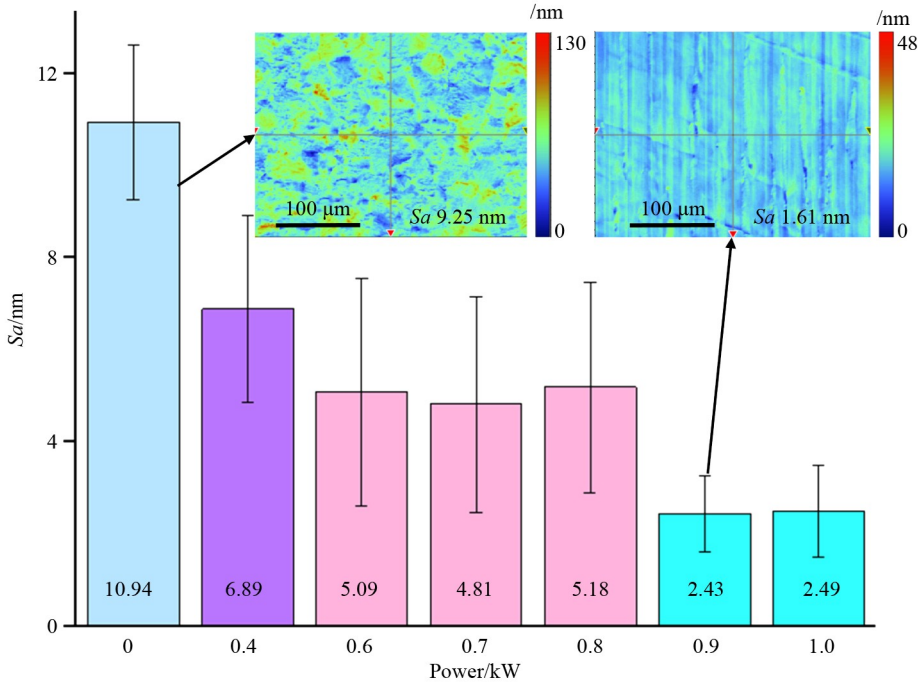

Fig. 9 Surface roughness in *Sa* of the polycrystalline tin samples modified using different powers.

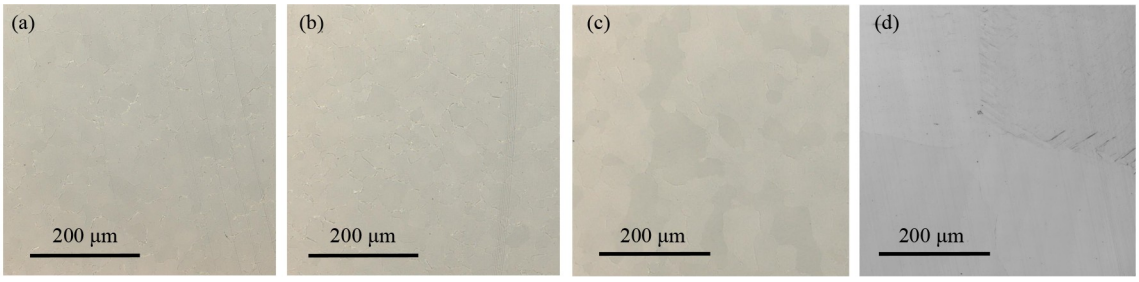

Fig. 10 Laser confocal microscope images of the polycrystalline tin samples modified using different radio frequency powers: (a) 0 kW, (b) 0.4 kW, (c) 0.7 kW, and (d) 0.9 kW.

gradient, the grain size gradually expanded from 20–40 to 400–500 μm, which showed that a *GranT* of about 0.30 K/μm was conducive to the grain growth. The trends of surface roughness and temperature gradient of the corresponding four groups in Fig. 9 after SPDT were opposite.

The surface grain distribution and size of the control and 0.9 kW-modified group surfaces after SPDT were characterized by EBSD further. The unmodified polycrystalline tin retained a large number of GBs after SPDT, as shown in Figs. 11(a)–11(c). The grain sizes were distributed between 20 and 200 μm, and substantial misorientations were observed, as shown in Fig. 11(c). After modification, the grain size increased significantly to greater than 500 μm, and the misorientations were effectively removed, as shown in Figs. 11(d)–11(f). The comparison revealed that the grain size increased significantly after ICP modification.

The above experimental results showed that the grain size of polycrystalline tin increased significantly after the modification by ICP treatment with a *GranT* of 0.30 K/μm, and the influence of grain steps on surface quality was effectively restrained, which strongly proved the feasibility of PaC for polycrystalline tin. The optimal power for ICP modification was 0.9 kW.

3.2 SPDT parameter optimization

The ANOVA can effectively separate the relevant factors and estimate their effect on the processing results. Hence, it was used to evaluate the importance of the influences on the surface roughness in *Sa* at a 95% confidence level based on the WL measurement data (Table 4).

The *p*-value indicates the importance of factors. This value is inversely related to the influence of weight. The *p*-values of rotational speed, feed rate, and cut depth were 0.015, 0.263, and 0.516, respectively. The *p*-value of rotational speed was considerably less than those of the

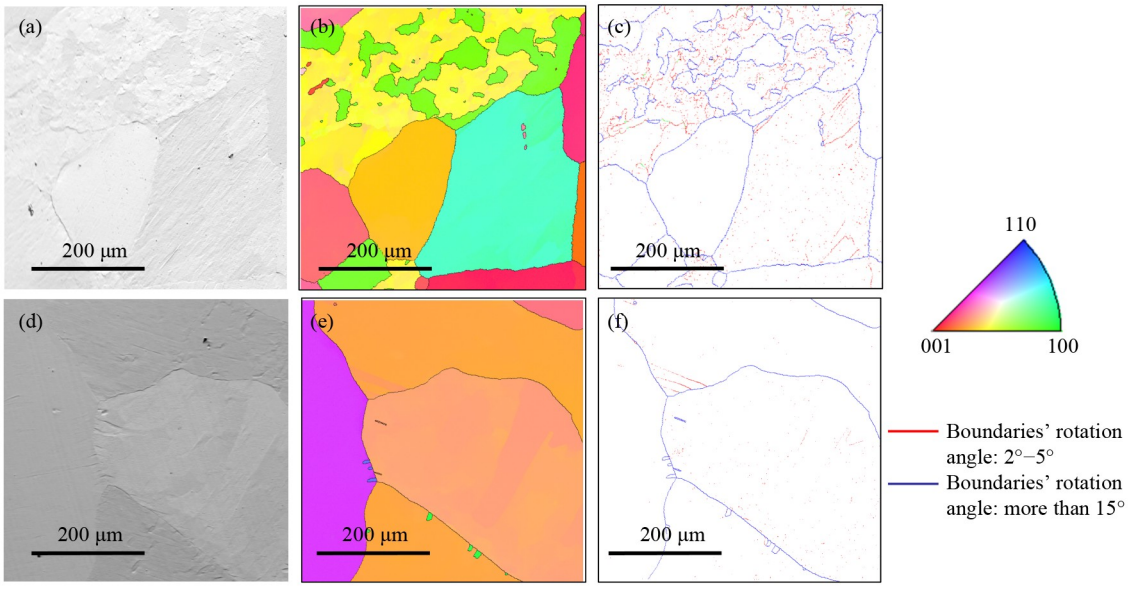

Fig. 11 Characterization of the polycrystalline tin surface: (a) scanning electron microscopy image of the 500 μm × 500 μm area in the unmodified sample, (b) electron backscatter diffraction inverse pole figure of the same surface in (a), (c) grain boundary inverse pole figure of the same surface in (a), (d) scanning electron microscopy image of the 500 μm × 500 μm area in the modified sample, (e) electron backscatter diffraction inverse pole figure of the same surface in (d), and (f) grain boundary inverse pole figure of the same surface in (d).

Table 4 ANOVA results from the mean surface roughness

Factors	Degree of freedom	Sum of squares	Mean of squares	*F*-value	*p*-value	Contribution rate/%
Rotational speed	2	7.440	3.720	67.010	0.015	93.40
Feed rate	2	0.311	0.155	2.801	0.263	3.90
Depth of cut	2	0.104	0.052	0.938	0.516	1.31
Error	2	0.111	0.056	–	–	1.39
Total	8	7.966	–	–	–	–

other two factors, which implied that the rotational speed of the machine was the most influential factor. The contribution rate of the blank group (1.39%) was similar to that of the depth of cut (1.31%). Thus, the influence of the depth of cut was insignificant within the range of parameter design. The feed rate showed a certain influence, but the contribution rate was only 3.90% [33].

The signal-to-noise (S/N) ratio reflects the experimental parameters' stability, which was used in the optimization of the control factors. In the Taguchi method, a small surface roughness in *Sa* was expected [39]. The influence of individual variables on surface roughness in *Sa* was investigated (Table 5). According to the analysis results, 2000 r/min rotational speed, 0.9 μm/r feed rate, and 0.6 μm depth of cut exhibited the maximum S/N ratio. The delta of the blank group (0.849 dB) was similar to that of the depth of cut (0.710 dB) and notably smaller than the most influential factor, that is, rotational speed (6.145 dB), verifying the validity of the Taguchi method design.

To optimize the parameters, we calculated the differences in surface roughness in *Sa* for various factors at the same level (Table 6). The delta of the blank group was similar to the depth of cut and had a small value, establishing the experimental validity. The results showed that the 2000 r/min rotational speed obtained the minimum surface roughness in *Sa*. As the rotational

Table 5 S/N response table for the surface roughness

Factors	S/N ratio/dB			Delta
	Level 1	Level 2	Level 3	
Rotational speed	−10.718	−6.700	−12.845	6.145
Feed rate	−9.394	−10.205	−10.664	1.269
Depth of cut	−9.851	−9.851	−10.561	0.710
Blank group	−10.510	−10.092	−9.661	0.849

Table 6 Average surface roughness in *Sa*

Factors	*Sa*/nm			Delta
	Level 1	Level 2	Level 3	
Rotational speed	3.440	2.117	4.397	2.220
Feed rate	3.123	3.313	3.577	0.453
Depth of cut	3.203	3.343	3.467	0.263
Blank group	3.487	3.307	3.220	0.267

speed increased, the strain rate of the polycrystalline tin increased, resulting in material strengthening [40], and the influence of low hardness was reduced. The serious deterioration in surface quality at 3000 r/min rotational speed was attributed to two main reasons. First, with the increase in rotational speed, the cutting temperature increased gradually. When the rotational speed was raised from 2000 to 3000 r/min, the surface heat storage could not diffuse effectively, melting occurred on the machined tin surface, and microdefects, such as scratches, appeared on the surface. Second, the adjustment of dynamic balance became more difficult with the increase in speed, resulting in chatter marks on the surface.

Scratches and chatter marks were observed on the surface of the polycrystalline tin, and the surface roughness in *Sa* was 6.11 nm in Fig. 12(a). The surface quality decreased as the feed speed increased. The feed rate of 0.9 μm/r was the optimal value for polycrystalline tin machining. A lower feed rate resulted in a smaller undeformed chip thickness (UCT), which improved the surface quality. In addition, the 0.6 μm cut depth had a low surface roughness. Xue et al. [11] found that single-crystal tin released high compressive stress under the tool pressure by slip, phase transformation, and amorphization. The increase in UCT increased the slip and phase transformation via molecular dynamics. However, the depth of cut effect of the experiment only exerted a minimal influence on surface roughness within the stated level. Many folds appeared on the machined surface at a cut depth of 2 μm, as shown in Fig. 12(b). The surface roughness in *Sa* was 1.33 nm, but many GB steps with a height of approximately 8 nm and a grain size of 80–100 μm were observed. To confirm the angular difference between grains under the 2 μm depth of cut, we carried out EBSD characterization on the sample surface (Fig. 12(b)). The grain size of tin was similar to that in Fig. 12(b), indicating that grains were produced after processing under a large depth of cut, as illustrated in Figs. 13(a)–13(c). The GB rotation angle ranged from 2° to 5°, indicating a small-angle GB. The above results showed that as the cut depth and UCT increased, many subgrains with sizes of 80–100 μm appeared in the larger grains (millimeter-scale) of polycrystalline tin. This finding might be due to the increase in UCT, which caused dislocation slips on the surface of polycrystalline tin [41,42].

The optimal parameters for processing ICP-modified polycrystalline tin surface were a rotational speed of 2000 r/min, a feed rate of 0.9 μm/r, and a cut depth of 0.6 μm. The unmodified polycrystalline tin and plasma-modified polycrystalline tin with a power of 0.9 kW were selected for the orthogonal optimal-parameter SPDT experiment. The surface roughness of the machined polycrystalline tin obtained with the new PaC method was less than 1 nm in *Sa*, and only cutting patterns could be observed in the inner region of the polycrystalline tin grain. The surface roughness was 0.80 nm (Fig. 14(a)). GB steps were detected at the junction of two

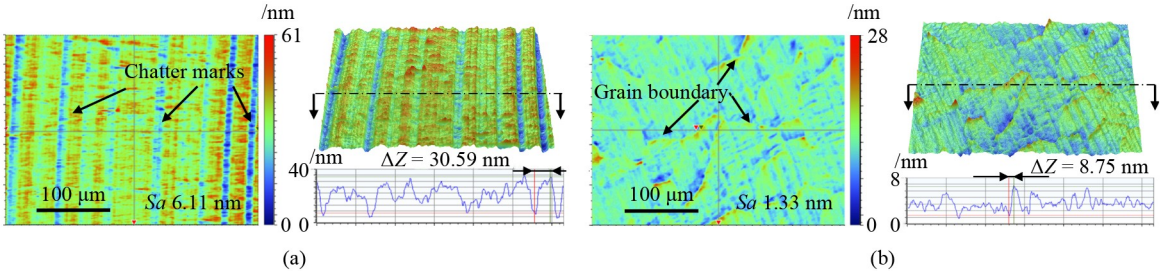

Fig. 12 Surface roughness under different parameters: (a) rotational speed of 3000 r/min, feed rate of 1.8 μm/r, and cut depth of 0.6 μm and (b) rotational speed of 2000 r/min, feed rate of 0.9 μm/r, and cut depth of 2 μm.

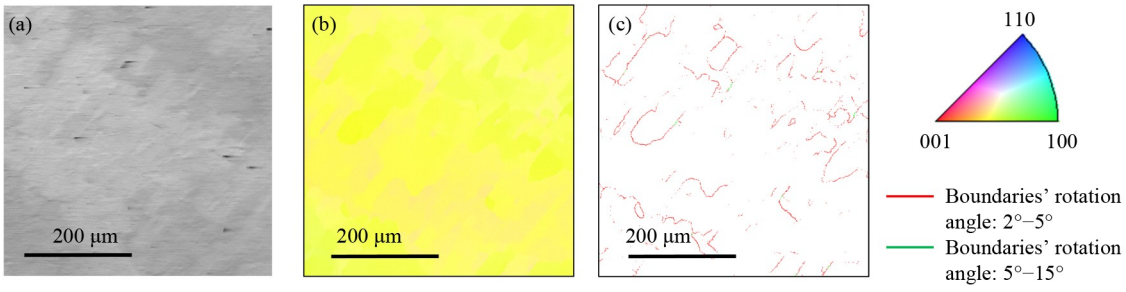

Fig. 13 Electron backscatter diffraction (EBSD) result of the sample in Fig. 14(b). (a) scanning electron microscopy image of the 500 μm × 500 μm area, (b) EBSD inverse pole figure of the same surface in (a), and (c) EBSD grain boundary image of the same surface in (a).

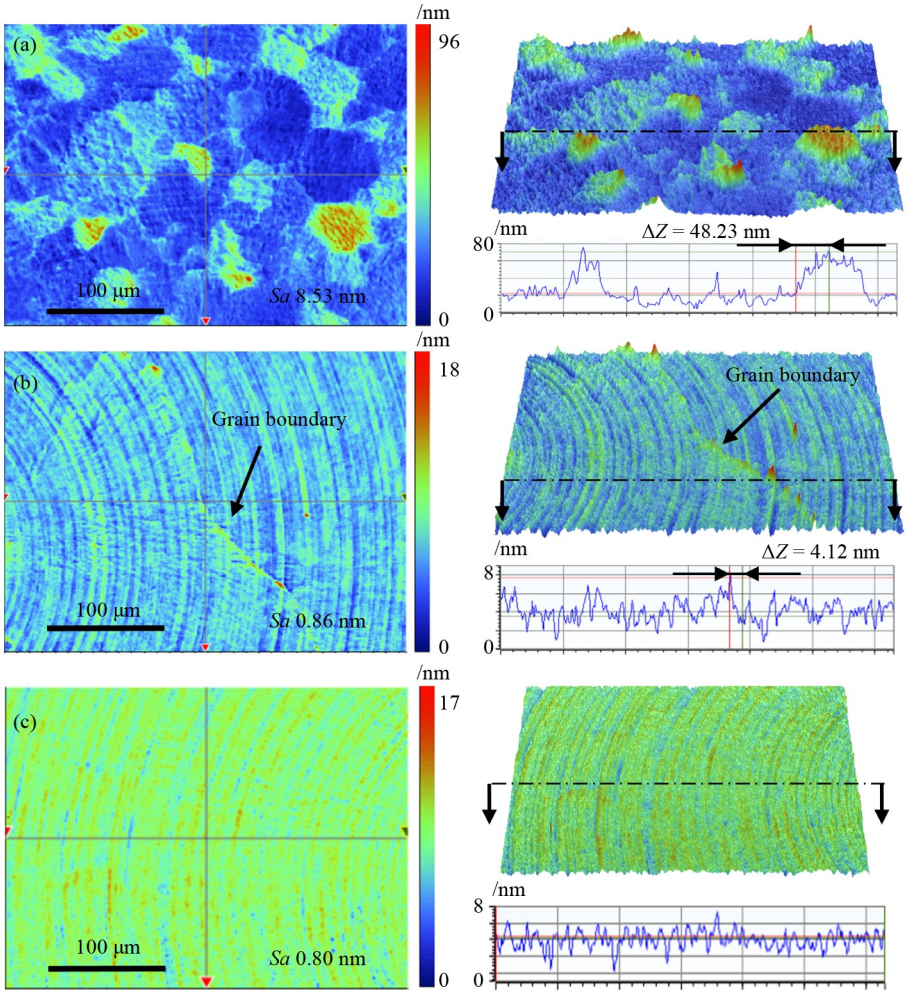

Fig. 14 Surface roughness in *Sa* under optimal orthogonal parameters: (a) without plasma treatment, (b) after 0.9 kW plasma treatment at the junction of two grains, and (c) after 0.9 kW plasma treatment in one grain.

polycrystalline tin grains, but the height of GB steps was 4.12 nm, which had a minor effect on the surface roughness (Fig. 14(b)). By contrast, substantial grains with a size of 40–80 μm appeared on the surface of the unmodified polycrystalline tin in Fig. 14(c). Given the different orientations and sizes of each grain, the types of GBs between various grains also differed, resulting in significant differences in the microstructure deformation of the machined surface grain. In addition, the elastic-plastic recovery of each grain was different after SPDT. The disparity in GB step height between different grains was evident, indicating that the surface quality was seriously affected. The surface roughness in *Sa* was 8.53 nm, and the GB step height was 48.23 nm. The above characterization results showed that the surface quality of the polycrystalline tin modified by ICP was improved greatly after optimized SPDT processing, and a surface roughness in *Sa* less than 1 nm was obtained, which proved the progressiveness of the PaC treatment. Figure 15 shows the photograph of the polycrystalline tin sample after processing with the optimal parameters of PaC.

3.3 Time-dependent changes in surface roughness and residual stress

Residual stress had an essential influence on the service life and surface quality of polycrystalline tin samples. Although the parameters of SDPT were optimized and a small cut depth and an appropriate spindle speed were selected, residual stress was inevitably introduced onto the surface of polycrystalline tin in the process of mechanical removal. The process of stress release was reflected in the change in the surface state.

The surface roughness of the polycrystalline tin samples machined using the PaC method and traditional SPDT (Fig. 15) was observed at fixed points to explore the changes in the surface quality within 504 h. In particular, because the stress release process was accompanied by the change in the sample face shape, the measured data were not filtered. Figure 16 depicts the WL interferometer results of tin during 504 h.

After PaC processing, the surface quality showed minimal changes in one of the polycrystalline tin grains.

As shown in Fig. 16(a), the surface roughness in *Sa* increased from 0.8 to 0.87 nm. The measurement result after 504 h is shown in Fig. 16(d). Considerable noise, which was caused by the residual dust on the surface during placement, was observed at the measuring points after 504 h standing and had a minor effect on the entire surface. At the junction of two polycrystalline tin grains shown in Fig. 16(b), the interaction between grains caused the lifting of the left grain and increased the grain step height from 4.12 to 30.26 nm. The surface roughness increased significantly in the first 36 h and then changed slowly, indicating that the stress gradually became stable after a short-time release. The final surface roughness in *Sa* was 2.56 nm (Fig. 16(e)). The structure at the GB of polycrystalline tin was different from that inside the grain, and the structures at the GBs were unstable. The surface change caused by stress release exerted a slight effect on the grain interior but caused an evident fluctuation effect at the GBs, which was similar to the SPDT of other polycrystalline metals [12–14]. By contrast, a drastic change was observed on the surface of the unmodified polycrystalline tin (Fig. 16(c)), in which the surface roughness increased from 8.53 to 12.06 nm in the first 48 h and then changed very slowly. The final surface roughness was 12.30 nm (Fig. 16(f)). The change trend of the surface roughness was consistent with that shown in Fig. 16(b). From the final WL image in Fig. 16(f), a remarkable interaction occurred between the grains. The grains contained numerous folds, and the GB step increased from 48.23 to 61.28 nm.

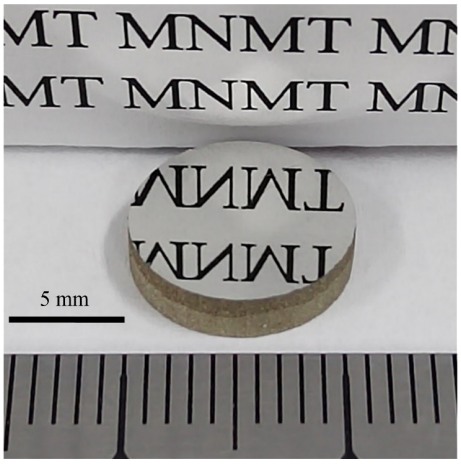

Fig. 15 Photograph of polycrystalline tin after processing with the optimal parameters of plasma-assister cutting.

The stress distribution in the workpieces machined by PaC and traditional SPDT after 72 and 504 h standing was measured (Pulstec U360). Three random areas in the two samples with an aperture of 1 mm were measured by X-ray diffraction [43,44]. The Debye ring images are shown in Fig. 17. The residual stresses of the two samples after standing for 72 h were the same as those after standing for 504 h, indicating that the majority of residual

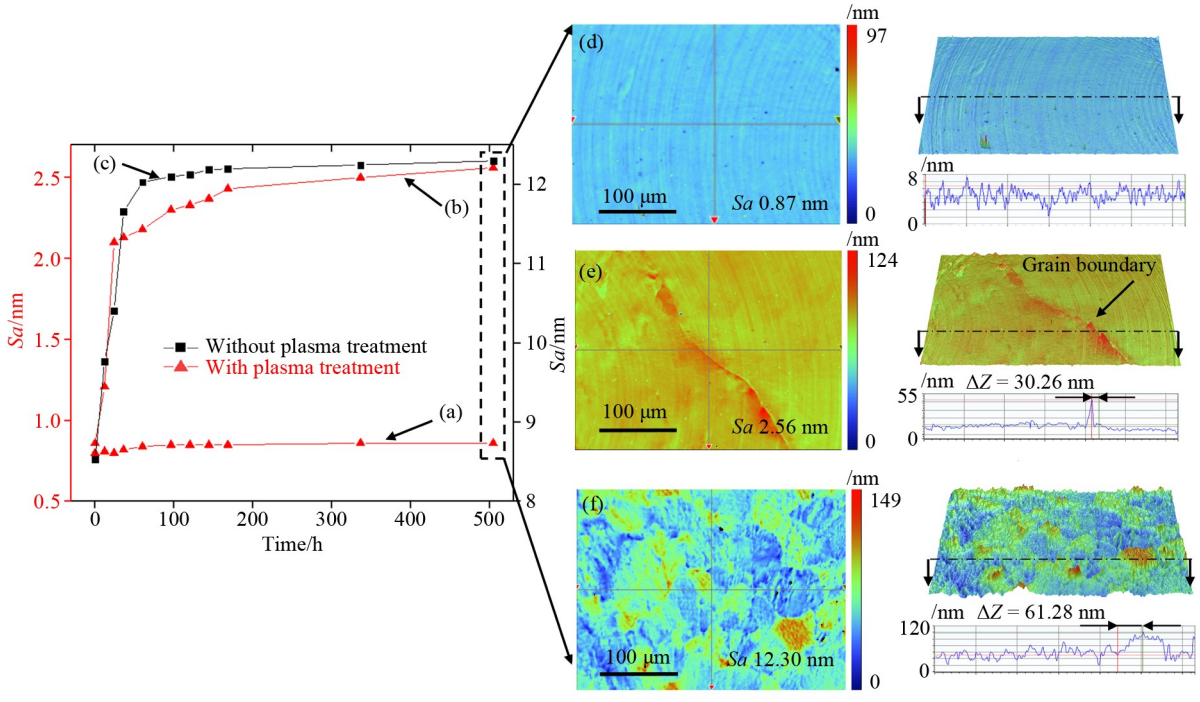

Fig. 16 Surface roughness in *Sa* under optimal parameters: (a) after 0.9 kW plasma treatment in one of the grains during 504 h standing, (b) after 0.9 kW plasma treatment at the junction of two grains during 504 h standing, (c) without plasma treatment during 504 h standing, (d) after 0.9 kW plasma treatment in one of the grains after 504 h standing, (e) after 0.9 kW plasma treatment at the junction of two grains after 504 h standing, and (f) without plasma treatment after 504 h standing.

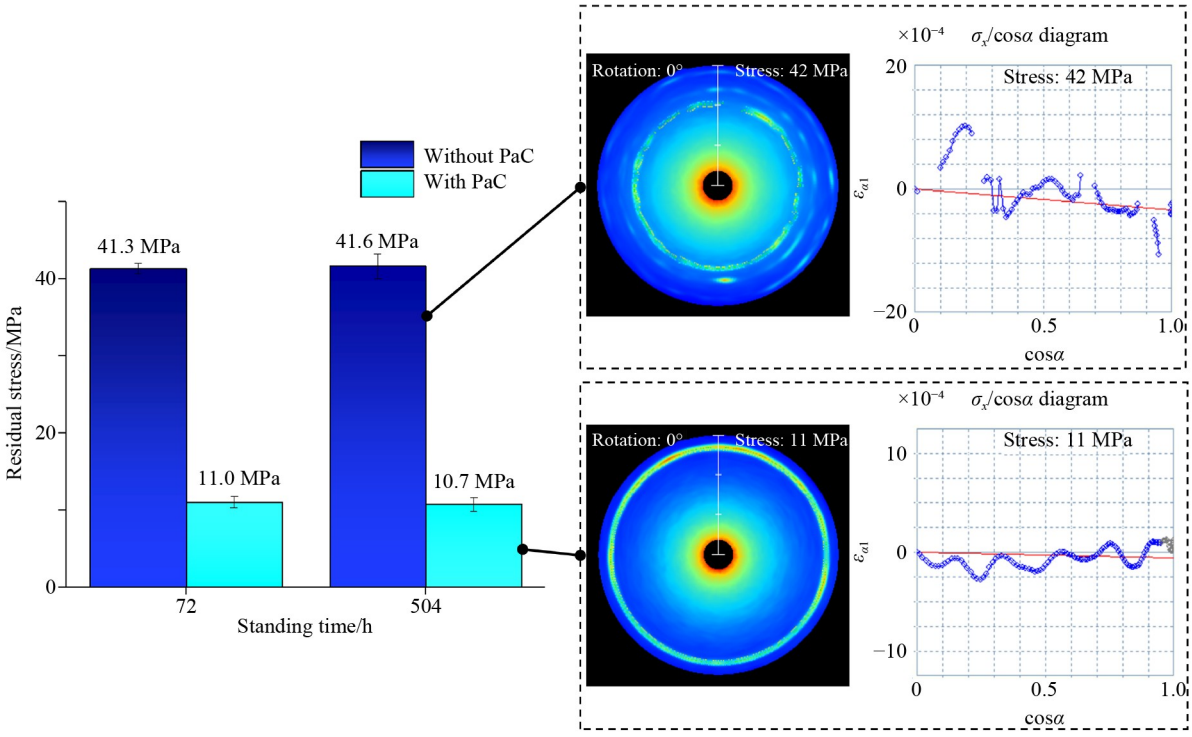

Fig. 17 Residual stress comparison of workpieces with and without PaC processing after standing for 72 and 504 h. PaC: plasma-assisted cutting.

stress had been released in the first 72 h. This finding corresponded to the deterioration of the surface roughness in the first 72 h. In addition, almost no change occurred from 72 to 504 h standing (Fig. 16), implying that the increase in surface roughness was the result of stress release. The residual stress of the PaC-processed tin was 10.7 MPa after being fully released, which was smaller than the 41.6 MPa observed in the traditional SPDT process. After the polycrystalline tin samples processed using the new method were left to stand for 504 h, the surface residual stress and the change in surface roughness were reduced, which proved that the PaC method could effectively reduce the stress of polycrystalline tin under the same turning parameters and improve the service life of the workpiece. The Debye ring measured results of the two samples are shown on the right of Fig. 17, illustrating the uneven distribution of the Debye ring in the traditional SPDT process. Breakpoints were observed in the cosα diagram (α means the central angle of each point on the Debye ring), which might be due to the discontinuity caused by different grain steps and directions. On the contrary, the Debye ring was evenly distributed, and the cosα diagram was continuous after processing by the PaC process.

The above results showed that PaC can be employed to expand the grain size from 20 μm to a millimeter scale, effectively reducing the residual stress caused by SPDT. Cutting was carried out in different grains and was discontinuous. The hardness of polycrystalline tin is low, and it is easy to deform at the GB during processing, which leads to the reduction of its reliability and service performance [45,46]. When the grain size is small for oxygen-free Cu and other soft polycrystalline materials, the anisotropy of the grain causes large residual stress [47], which is consistent with the phenomenon observed in Fig. 17.

4 Conclusions

A novel method combining ICP and SPDT was developed to achieve a sub-nanometer surface finish of polycrystalline tin. The irradiation of ICP provided a large temperature gradient on the surface of polycrystalline tin, and a grain fusion-modified layer was obtained in several seconds, which greatly reduced the effect of GB steps on the machined surface roughness of polycrystalline tin obtained by SPDT processing. The machining residual stress introduced by SPDT was also effectively reduced. The modification method of using the large thermal gradient of ICP to irradiate the metal surface to increase the grain size can further be applied to the SPDT processing of other metal materials.

(1) The established thermodynamic simulation models can be utilized to characterize material alterations caused by ICP. The fitted heat transfer coefficient of polycrystalline tin (540 W/(m^2·K)) can effectively guide the selection of plasma modification parameters. The ICP

modification time was 3.0 s for the samples with a diameter of 10 mm, and the depth of the modified layer was 1.24 mm at the center of the sample.

(2) The developed PaC device eliminates the requirement for a vacuum chamber and is thus cost-effective. The PaC method was verified as an efficient modification method for sub-nanometer surface finishing. For polycrystalline tin samples with different diameters, the size of the plasma tube can be flexibly adjusted for efficient modification, which provides a new way for large-thermal-gradient treatment on the surface of soft metal surface.

(3) Different plasma irradiation powers corresponded to various temperature gradients, which played an important role in the fusion growth of polycrystalline tin grains. With the increase in temperature gradient from 0.12 to 0.32 K/μm, the effect of grain fusion improved. The optimal plasma RF power for modification was 0.9 kW, corresponding to the temperature gradient of 0.30 K/μm and increasing the grain size from 20 to more than 500 μm.

(4) The optimized SPDT process parameters of a rotational speed of 2000 r/min, a depth of cut of 6 μm, and a feed rate of 0.9 μm/r were used to achieve low surface roughness and maximum S/N ratio. Compared with the traditional SPDT process, the optimized SPDT process achieved a significant reduction in surface roughness from 8.53 to 0.80 nm in *Sa*.

(5) After SPDT processing, the stress release time of polycrystalline tin became independent of the grain size, and the stress release was completed after 72 h standing. The surface roughness of the sample subjected to the PaC process was unchanged in the grain but deteriorated to 2.56 nm because of the rise in GB steps at the junction of two polycrystalline tin grains. The corresponding surface roughness without surface modification deteriorated from 8.53 to 12.30 nm in *Sa*. Furthermore, the residual stress after standing for 504 h was only 10.7 MPa, which was approximately one-quarter of that of the unmodified sample under the same conditions. Hence, polycrystalline tin samples with low surface stress were achieved.

Nomenclature

Abbreviations

ACS	Atomic and close-to-atomic scale
Al	Aluminium
ANOVA	Analysis of variance
Ar	Argon
Cu	Copper
EBSD	Electron backscatter diffraction
EBSM	Electron beam selective melting
GB	Grain boundary
ICP	Inductively coupled plasma
PaC	Plasma-assisted cutting
RF	Radio frequency
SEM	Scanning electron microscopy
S/N	Signal-to-noise
SPDT	Single-point diamond turning
UCT	Undeformed chip thickness
WL	White light

Variables

A	Height of Gaussian function
B	Offset of the Gaussian function along the y-axis
C_P	Plasma's specific heat capacity
C_p1	Tin's specific thermal capacity
$\boldsymbol{F}$	Lorentz force
$GranT$	Initial temperature gradient
h	Coefficient of heat transfer
$\boldsymbol{I}$	Matrix of identity
k	Thermal conductivity
k_1	Thermal conductivity of tin
$\boldsymbol{n}$	Normal vector
p	Pressure
q_0	Internal heat flow
$\boldsymbol{q}$	Plasma's heat flux conductivity vector
$\boldsymbol{q}_1$	Vector of heat flux conductivity
Q	Source of heat
Q_1	Heat source of tin
Q_p	Work of pressure
Q_ted	Thermoelastic damping
Q_vd	Work of viscous dissipation
T	Plasma temperature
T_1	Temperature of tin
T_bottom	Bottom temperature of polycrystalline tin
T_ext	ICP action section temperature
T_ext0	Central temperature of the heat source
$\boldsymbol{u}$	Plasma's velocity vector
$\boldsymbol{u}_1$	Tin's velocity vector
α	Central angle of each point on the Debye ring
ρ	Plasma's fluid density
ρ_1	Density of tin
μ	Dynamic viscosity
σ	Standard deviation of the Gaussian function

Acknowledgements The authors would like to thank the financial support from the National Natural Science Foundation of China (Grant No. 52035009), the Science Challenge Project, China (Grant No. TZ2018006-0201-01), the National Key R&D Program of China (Grant No. 2016YFB1102203), and the "111" project by the State Administration of

Foreign Experts Affairs and the Ministry of Education of China (Grant No. B07014).

Funding Note Open Access funding provided by the IReL Consortium.

Conflict of Interest The authors declare that they have no conflict of interest.

References

1. Beaucamp A T H, Nagai K, Hirayama T, Okada M, Suzuki H, Namba Y. Elucidation of material removal mechanism in float polishing. Precision Engineering, 2022, 73: 423–434
2. White E, O'Sullivan G, Dunne P. Soft X-ray spectra of cerium laser-produced plasmas. Journal of Physics B: Atomic, Molecular, and Optical Physics, 2021, 54(23): 235701
3. Bouza Z, Byers J, Scheers J, Schupp R, Mostafa Y, Behnke L, Mazzotta Z, Sheil J, Ubachs W, Hoekstra R, Bayraktar M, Versolato O O. The spectrum of a 1-μm-wavelength-driven tin microdroplet laser-produced plasma source in the 5.5–265.5 nm wavelength range. AIP Advances, 2021, 11(12): 125003
4. Grigoryev S Y, Dyachkov S A, Parshikov A N, Zhakhovsky V V. Limited and unlimited spike growth from grooved free surface of shocked solid. Journal of Applied Physics, 2022, 131(6): 065104
5. Flanagan R M, Meyers M A, Fensin S J. The role of pre-existing defects in shock-generated ejecta in copper. Journal of Applied Physics, 2021, 130(7): 075101
6. Wang Y Z, Geng Y Q, Li G, Wang J Q, Fang Z, Yan Y D. Study of machining indentations over the entire surface of a target ball using the force modulation approach. International Journal of Extreme Manufacturing, 2021, 3(3): 035102
7. Fang F Z. Atomic and close-to-atomic scale manufacturing: perspectives and measures. International Journal of Extreme Manufacturing, 2020, 2(3): 030201
8. Fang F Z. The three paradigms of manufacturing advancement. Journal of Manufacturing Systems, 2022, 63: 504–505
9. Zeng C Z, Shen J, Ma C F. Effect of diamond microparticles on the thermal behavior of low melting point metal: an experimental and numerical study. International Journal of Thermal Sciences, 2022, 178: 107613
10. Wang J, Xing J D, Wang D Y, Jiang H X. Research on the processing and performance of single crystal tin strips using a heated mould. Rare Metal Materials and Engineering, 2008, 9(37): 1160–1163
11. Xue Z F, Lai M, Xu F F, Fang F Z. Molecular dynamics study on surface formation and phase transformation in nanometric cutting of β-Sn. Advances in Manufacturing, 2022, 10(3): 356–367
12. Brinksmeier E, Gläbe R, Osmer J. Ultra-precision diamond cutting of steel molds. CIRP Annals, 2006, 55(1): 551–554
13. Brinksmeier E, Preuss W, Riemer O, Rentsch R. Cutting forces, tool wear and surface finish in high speed diamond machining. Precision Engineering, 2017, 49: 293–304
14. Wang Z F, Zhang J J, Li G, Xu Z W, Zhang H J, Zhang J G, Hartmaier A, Fang F Z, Yan Y D, Sun T. Anisotropy-related machining characteristics in ultra-precision diamond cutting of crystalline copper. Nanomanufacturing and Metrology, 2020, 3(2): 123–132
15. Liang S B, Ke C B, Wei C, Zhou M B, Zhang X P. Phase field modeling of grain boundary migration and preferential grain growth driven by electric current stressing. Journal of Applied Physics, 2018, 124(17): 175109
16. Tonks M R, Zhang Y F, Bai X M, Millett P C. Demonstrating the temperature gradient impact on grain growth in UO_2 using the phase field method. Materials Research Letters, 2014, 2(1): 23–28
17. Omori T, Kusama T, Kawata S, Ohnuma I, Sutou Y, Araki Y, Ishida K, Kainuma R. Abnormal grain growth induced by cyclic heat treatment. Science, 2013, 341(6153): 1500–1502
18. Xu X Z, Zhang Z H, Dong J C, Yi D, Niu J J, Wu M H, Lin L, Yin R K, Li M Q, Zhou J Y, Wang S X, Sun J L, Duan X J, Gao P, Jiang Y, Wu X S, Peng H L, Ruoff R S, Liu Z F, Yu D P, Wang E G, Ding F, Liu K H. Ultrafast epitaxial growth of metre-sized single-crystal graphene on industrial Cu foil. Science Bulletin, 2017, 62(15): 1074–1080
19. Zhang G H, Lu X F, Li J Q, Chen J, Lin X, Wang M, Tan H, Huang W D. *In-situ* grain structure control in directed energy deposition of Ti6Al4V. Additive Manufacturing, 2022, 55: 102865
20. Fernandez-Zelaia P, Kirka M M, Rossy A M, Lee Y, Dryepondt S N. Nickel-based superalloy single crystals fabricated via electron beam melting. Acta Materialia, 2021, 216: 117133
21. Zhang X C, Li W, Liou F. Additive manufacturing of cobalt-based alloy on tool steel by directed energy deposition. Optics & Laser Technology, 2022, 148: 107738
22. Li Y, Yu Y F, Wang Z B, Liang X Y, Kan W B, Lin F. Additive manufacturing of nickel-based superalloy single crystals with IN-738 alloy. Acta Metallurgica Sinica, 2022, 35(3): 369–374
23. Helmer H, Bauereiß A, Singer R F, Körner C. Grain structure evolution in Inconel 718 during selective electron beam melting. Materials Science and Engineering: A, 2016, 668: 180–187
24. Rai A, Helmer H, Körner C. Simulation of grain structure evolution during powder bed based additive manufacturing. Additive Manufacturing, 2017, 13: 124–134
25. Murphy A B, Uhrlandt D. Foundations of high-pressure thermal plasmas. Plasma Sources Science & Technology, 2018, 27(6): 063001
26. Indhu R, Vivek V, Sarathkumar L, Bharatish A, Soundarapandian S. Overview of laser absorptivity measurement techniques for

material processing. Lasers in Manufacturing and Materials Processing, 2018, 5(4): 458–481

27. Paparao J, Murugan S. Oxy-hydrogen gas as an alternative fuel for heat and power generation applications—a review. International Journal of Hydrogen Energy, 2021, 46(76): 37705–37735
28. Li R L, Li Y G, Deng H. Plasma-induced atom migration manufacturing of fused silica. Precision Engineering, 2022, 76: 305–313
29. Shibata Y, Sakairi Y, Shimada K, Mizutani M, Kuriyagawa T. Effects of topography and modified layer by plasma-shot treatment on high-speed steel. Nanomanufacturing and Metrology, 2020, 3(2): 133–141
30. Bennett A, Yu N, Castelli M, Chen G D, Balleri A, Urayama T, Fang F Z. Characterisation of a microwave induced plasma torch for glass surface modification. Frontiers of Mechanical Engineering, 2021, 16(1): 122–132
31. Zhang Y, Zhang L F, Chen K Y, Liu D Z, Lu D, Deng H. Rapid subsurface damage detection of SiC using inductivity coupled plasma. International Journal of Extreme Manufacturing, 2021, 3(3): 035202
32. Ji P, Jin H L, Li D, Su X, Liu K, Wang B. Thermal modelling for conformal polishing in inductively coupled atmospheric pressure plasma processing. Optik, 2019, 182: 415–423
33. Ayyıldız E A, Ayyıldız M, Kara F. Optimization of surface roughness in drilling medium-density fiberboard with a parallel robot. Advances in Materials Science and Engineering, 2021, 2021: 6658968
34. Lyu P, Lai M, Liu Z, Fang F Z. Ultra-smooth finishing of single-crystal lutetium oxide by plasma-assisted etching. Precision Engineering, 2021, 67: 77–88
35. Napolitano R E, Schaefer R J. The convergence-fault mechanism for low-angle boundary formation in single-crystal castings. Journal of Materials Science, 2000, 35(7): 1641–1659
36. Stanford N, Djakovic A, Shollock B A, Mclean M, Souza N D, Jennings P A. Seeding of single crystal superalloys—role of seed melt-back on casting defects. Scripta Materialia, 2004, 50(1): 159–163
37. Jo H K, Park H J, Lee H J, Bae G, Song D S, Kim K K, Song W, Jeon C, An K S, Kwon Y K, Park C Y. Oxygen-mediated selection of Cu crystallographic orientation for growth of single-crystalline graphene. Applied Surface Science, 2022, 584: 152585
38. Sun L Z, Chen B H, Wang W D, Li Y L Z, Zeng X Z, Liu H Y, Liang Y, Zhao Z Y, Cai A L, Zhang R, Zhu Y S, Wang Y C, Song Y Q, Ding Q J, Gao X, Peng H L, Li Z Y, Lin L, Liu Z F. Toward epitaxial growth of misorientation-free graphene on Cu (111) foils. ACS Nano, 2022, 16(1): 285–294
39. Nas E, Kara F. Optimization of EDM machinability of hastelloy C22 super alloys. Machines, 2022, 10(12): 1131
40. Zhang B, Yin J F. The skin effect of subsurface damage distribution in materials subjected to high-speed machining. International Journal of Extreme Manufacturing, 2019, 1(1): 012007
41. Wang Z F, Zhang J J, Zhang J G, Li G, Zhang H J, ul Hassan H, Hartmaier A, Yan Y D, Sun T. Towards an understanding of grain boundary step in diamond cutting of polycrystalline copper. Journal of Materials Processing Technology, 2020, 276: 116400
42. Xie G, Zhang S H, Zheng W, Zhang G, Shen J, Lu Y Z, Hao H Q, Wang L, Lou L H, Zhang J. Formation and evolution of low angle grain boundary in large-scale single crystal superalloy blade. Acta Metallurgica Sinica, 2019, 55(12): 1527–1536
43. You K Y, Fang F Z, Yan G P. Surface generation of tungsten carbide in laser-assisted diamond turning. International Journal of Machine Tools and Manufacture, 2021, 168: 103770
44. Mitsui S, Sasaki T, Arai Y, Miyoshi T, Nishimura R. Development of Debye-ring measurement system using SOI pixel detector. Nuclear Instruments & Methods in Physics Research Section A: Accelerators, Spectrometers, Detectors and Associated Equipment, 2019, 924: 441–447
45. Wu X, Li L, He N, Yao C J, Zhao M. Influence of the cutting edge radius and the material grain size on the cutting force in micro cutting. Precision Engineering, 2016, 45: 359–364
46. Nazari F, Honarpisheh M, Zhao H Y. The effect of microstructure parameters on the residual stresses in the ultrafine-grained sheets. Micron, 2020, 132: 102843
47. Ji R J, Zheng Q, Liu Y H, Jin H, Zhang F, Liu S G, Wang B K, Lu S C, Cai B P, Li X P. Effect of grain refinement on cutting force of difficult-to-cut metals in ultra-precision machining. Chinese Journal of Aeronautics, 2022, 35(3): 484–493